

# Analysis of large-amplitude stratospheric mountain wave event observed from the AIRS and MLS sounders over the western Himalayan region

K. Niranjana Kumar,<sup>1,2</sup> T. K. Ramkumar,<sup>3</sup> and M. Krishnaiah<sup>4</sup>

Received 27 December 2011; revised 26 July 2012; accepted 27 September 2012; published 16 November 2012.

[1] Mountain waves in the stratosphere have been observed over elevated topographies using both nadir-looking and limb-viewing satellites. However, the characteristics of mountain waves generated over the Himalayan Mountain range and the adjacent Tibetan Plateau are relatively less explored. The present study reports on three-dimensional (3-D) properties of a mountain wave event that occurred over the western Himalayan region on 9 December 2008. Observations made by the Atmospheric Infrared Sounder on board the Aqua and Microwave Limb Sounder on board the Aura satellites are used to delineate the wave properties. The observed wave properties such as horizontal ( $\lambda_x$ ,  $\lambda_y$ ) and vertical ( $\lambda_z$ ) wavelengths are 276 km (zonal), 289 km (meridional), and 25 km, respectively. A good agreement is found between the observed and modeled/analyzed vertical wavelength for a stationary gravity wave determined using the Modern Era Retrospective Analysis for Research and Applications (MERRA) reanalysis winds. The analysis of both the National Centers for Environmental Prediction/National Center for Atmospheric Research reanalysis and MERRA winds shows that the waves are primarily forced by strong flow across the topography. Using the 3-D properties of waves and the corrected temperature amplitudes, we estimated wave momentum fluxes of the order of  $\sim 0.05$  Pa, which is in agreement with large-amplitude mountain wave events reported elsewhere. In this regard, the present study is considered to be very much informative to the gravity wave drag schemes employed in current general circulation models for this region.

**Citation:** Niranjana Kumar, K., T. K. Ramkumar, and M. Krishnaiah (2012), Analysis of large-amplitude stratospheric mountain wave event observed from the AIRS and MLS sounders over the western Himalayan region, *J. Geophys. Res.*, 117, D22102, doi:10.1029/2011JD017410.

## 1. Introduction

[2] Gravity waves (GWs) play important roles in determining the general circulations and thermal structures of the atmosphere [e.g., Lindzen, 1981; Holton, 1982]. They are particularly important in the stratosphere and mesosphere, where they dissipate and deposit their momentum fluxes to the mean flow. Gravity waves are mostly generated in the lower troposphere by a variety of mechanisms [Fritts and Alexander, 2003]. Of these, the mountain waves generated by airflow over topography are believed to be one of the dominant sources particularly in the extratropics during

winter [Nastrom and Fritts, 1992]. Moreover, mountain waves can transport significant momentum and energy vertically up through the atmosphere and the effect of which is essential to understand the middle atmosphere circulation and chemistry [Haynes, 2005; Bacmeister, 1993; Carslaw et al., 1998; Dornbrack et al., 2001; Fueglistaler et al., 2003; Eckermann et al., 2006]. There is a wealth of literature (including some important reviews) existing on this subject [Queney, 1947; Smith, 1979, 1989; Blumen, 1990; Baines, 1995; Wurtele et al., 1996; Smith et al., 2002; Fritts and Alexander, 2003; Kim et al., 2003]. The influences of orographic gravity wave drag on the climate and meteorology of the extratropical winter stratosphere and mesosphere, the Polar Stratospheric Cloud (PSC) formation and the ozone loss must be parametrized in global middle atmosphere models [e.g., McLandress, 1998; Pierce et al., 2003; Mann et al., 2005; Siskind et al., 2007]. However, constraints are lacking for the present parameterizations in global climate models to assess the resulting effects, especially the dynamics of short-scale waves [Eckermann et al., 2007].

[3] Modeled gravity wave properties require observational verification that is difficult to obtain. However, recent advances in satellite-based remote-sensing technology

<sup>1</sup>Divecha Centre for Climate Change, Indian Institute of Science, Bangalore, India.

<sup>2</sup>Formerly at National Atmospheric Research Laboratory, Department of Space, Government of India, Gadanki, India.

<sup>3</sup>National Atmospheric Research Laboratory, Gadanki, India.

<sup>4</sup>Department of Physics, Sri Venkateswara University, Tirupati, India.

Corresponding author: K. Niranjana Kumar, Divecha Centre for Climate Change, Indian Institute of Science, Bangalore 560012, India. (niranjana@caos.iisc.ernet.in)

Published in 2012 by the American Geophysical Union.

**Table 1.** AIRS Channels Used for Present Study

SNO	AIRS Channel	Frequency ( $\text{cm}^{-1}$ )	$\text{NeN}^a$ ( $\text{mW/m}^2/\text{cm}^{-1}/\text{steradian}$ )
1	1986	2296.7	0.0027
2	2006	2316.9	0.0048
3	2081	2361.1	0.0015
4	75	667.78	0.5077

<sup>a</sup>Noise equivalent radiance for each channel for an assumed 250 K scene.

coupled with some innovative analysis techniques provide valuable information on small-scale gravity waves and their global properties throughout the atmosphere [Fetzer and Gille, 1994; Wu and Waters, 1996; Eckermann and Preusse, 1999; Tsuda et al., 2000; Wu, 2004]. Gravity wave momentum fluxes derived from these are normally used to constrain gravity wave parameterization in global models. However, estimations of wave momentum flux derived from satellite observations could not provide the needed constraints [Alexander and Barnett, 2007]. One reason is that estimation of wave momentum flux requires simultaneous observation of vertical and horizontal wavelengths and wave propagation direction [Ern et al., 2004]. Satellite-based instruments now offer appreciable resolution and precision for observing mesoscale gravity wave characteristics that can lead to reduced uncertainties in estimating momentum fluxes. Space-based observations also, in some cases, can provide detailed three-dimensional view of gravity waves (e.g., mountain waves) [Wu and Zhang, 2004; Eckermann et al., 2006; Alexander and Teitelbaum, 2007, 2011]. Using nadir-looking and limb-scanning satellite measurements, mountain waves have been observed over several parts of the world such as Antarctic Peninsula, Scandinavia, South Georgia Island, Andes, etc. [Eckermann et al., 2007; Alexander and Teitelbaum, 2007; Alexander et al., 2009; Eckermann and Preusse, 1999; Preusse et al., 2002; Alexander et al., 2008; Pitts et al., 2011]. However, the Himalayan region, and the adjacent Tibetan plateau, is less explored even though it comprises complex mountain ranges. This region also has profound dynamical and thermodynamic influences, affecting both the local and global climates [Boos and Kuang, 2010; Molnar et al., 2010]. They act as a physical barrier to the flow of air, leading to forcing of small-scale gravity waves to planetary-scale waves that can modify the atmospheric circulation [Trenberth and Chen, 1988; Barros et al., 2004]. In the present study, we analyzed a mountain wave event that occurred under the influence of strong westerlies flowing over the Himalayan region during a winter season. Gravity waves grow into significant strengths at places where the westerly wind was consistently strong from the lower troposphere to the upper stratosphere. The mountain wave event considered in the present study occurred during the winter season on 9 December 2008. The typical zonal wind structure that occurred during the winter over this region adjacent to the southwest of Tibetan plateau does not favor for the propagation of mountain gravity waves [Gong et al., 2011]. However, during this particular event, we observed weak wind changing its direction all over the troposphere that could favor mountain wave propagation into the stratosphere. The present study would be much informative to the gravity wave parameterization schemes as the Tibetan plateau is not very much dealt with in current GCMs [Kim et al., 2003]. The three-dimensional

(3-D) properties of mountain wave event occurred over the western Himalayan mountain region are analyzed using the measurements made from the AIRS and MLS sounder instruments. The following sections provide information about the data sources, results, and summary of the present study.

## 2. Data Sources

### 2.1. Atmospheric Infrared Sounder

[4] The present study makes use of retrievals from the space-borne instruments Atmospheric Infrared Sounder (AIRS) and Atmospheric Microwave Sounding Unit (AMSU). The AIRS/AMSU system on board the National Aeronautics and Space Administration (NASA) Aqua satellite was launched in 2002. The AIRS is the first of new-generation operational remote sensors for upwelling atmospheric emission [Aumann et al., 2003]. The AIRS and AMSU are cross-track-scanning nadir sounders (coaligned) and have a swath of  $\sim 1650$  km wide. With more than 2000 channels covering 3.71–4.61, 6.2–8.22, and 8.8–15.4  $\mu\text{m}$  in infrared bands, the AIRS can sense atmospheric temperature, water vapor, trace gases, and surface skin temperature with very high accuracies. Here, we make use of both the AIRS L1B (AIRS Level1B) radiance measurements and AIRS L2 (AIRS Level 2) temperature retrievals to study gravity wave perturbations. The AIRS footprint at nadir is 13.5 km and that of AMSU is 40.5 km. The AIRS L1B radiance measurements have higher horizontal resolution than the AIRS L2 retrievals. The temperature retrievals are based on from both the AIRS and AMSU retrievals and hence the AIRS-L2 temperature retrievals are of coarse resolution. In the present study, we examined radiance measurements obtained in the two  $\text{CO}_2$  bands centered at  $\sim 15$  and  $\sim 4.2$   $\mu\text{m}$ . The AIRS channels and the radiance noise for each channel are shown in Table 1. The horizontal resolution to study the gravity wave perturbations is high in radiance measurements in these two bands, but the vertical resolution is poor because of the broad vertical-scale weighting functions employed. Basically, the weighting functions reveal the extent to which the brightness temperature, measured by a particular frequency channel, is sensitive to the kinetic temperature that is a function of altitude. More details on the AIRS weighting functions for different frequency channels and their sensitivity to gravity wave characteristics can be found in Hoffmann and Alexander [2009] and Choi et al. [2012]. Each AIRS channel has distinct noise characteristics represented by Noise equivalent temperature ( $\text{NE}\delta T$ ). The  $\text{NE}\delta T$  of individual channels varies in the ranges of 0.14–0.19 K and 0.33–0.39 K for the 4.2 and 15  $\mu\text{m}$  channels, respectively [Aumann et al., 2000]. Also the error for the retrieved L2 temperature varies from 0.5 K to 2.5 K in the stratosphere.

[5] Removal of the background variations from each AIRS granule is essential to investigate small-scale gravity waves. Each AIRS granule contains a  $90 \times 135$  pixel image, covering a domain of approximately  $1600 \times 2300$  km. The cross-track pixel,  $\Delta x$ , varies in dimension with scan angle  $\theta$ . The size of each pixel is given approximately by  $\delta_o/\cos\theta$  and the along-track dimension ( $\Delta y$ ) is by  $\delta_o/\cos(1.4\theta)$ ;  $\delta_o = 13.5$  km is the nadir size on the ground. Prior to studying small-scale wave perturbations, the Limb brightening effect visible in raw radiance data must be

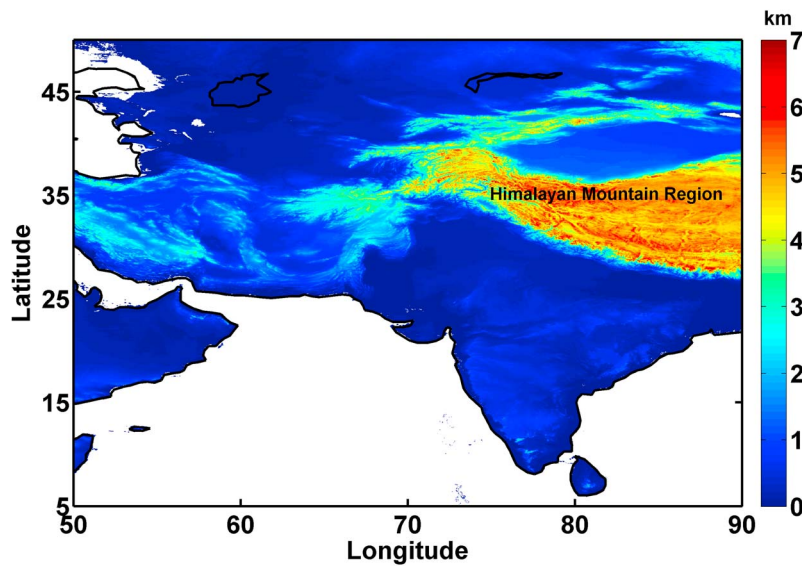


**Figure 1.** Topography map of the Himalayan mountain region generated using Shuttle Radar Topography Mission (SRTM) data. SRTM is an international project spearheaded by the National Geospatial-Intelligence Agency (NGA) and the National Aeronautics and Space Administration (NASA).

removed, occurring as a result of systematic scan angle dependence in the cross-track direction. A fourth order polynomial fit of the scan angle in the cross-track direction at each of the along-track positions is used to remove this effect [Wu, 2004]. The fit is subtracted from the raw radiances to obtain a residual field that resembles the atmospheric variability. The fourth-order polynomial fit also removes large-scale wave perturbations and thus limits our observations to wavelengths less than 500 km [Alexander and Barnett, 2007].

## 2.2. Microwave Limb Sounder

[6] As a supplement to the utilization of AIRS measurements, it is also used the temperature measured by the Microwave Limb Sounder (MLS) on board the Aura spacecraft. Details of the MLS instrument can be found in Waters *et al.* [2006]. The Aura spacecraft was launched on 15 July 2004 in near-polar, Sun-synchronous orbit. The spacecraft was located at the height of 705 km with equator-crossing local time of  $\sim 13:45$  LST (Local Standard Time) on the ascending node. MLS observes thermal microwave emission by the atmosphere in five spectral regions from 115 GHz to 2.5 THz. Aura MLS version 2.2 temperature data are used in this study. The MLS v2.2 product is described in Livesey *et al.* [2007]. Temperature is retrieved from bands near the  $O_2$  spectral lines at 118 GHz and 239 GHz that are detected by the MLS radiometers. The estimated precision of single temperature profile at the stratospheric heights is 0.6–1 K. The vertical resolution varies between 3.5 and 7.9 km. A detailed validation of the MLS v2.2 products and comparison of those data with other data sets can be found in Froidevaux *et al.* [2008], Jiang *et al.* [2007], and Schwartz *et al.* [2008].

## 2.3. MERRA Analysis

[7] For the 9 December 2008 mountain wave event, use has also been made of the Modern Era Retrospective Analysis for Research and Applications (MERRA) wind and temperature

fields. MERRA is a reanalysis data of the satellite era (1979-present), which used the Goddard Earth Observing System (GEOS-5) data assimilation system. More details of the MERRA/GEOS-5 numerical model and data assimilation system are described in Rienecker *et al.* [2007], while Rienecker *et al.* [2011] describe the MERRA project. In the present study, we used the MERRA 3-D 6-hourly global data set with  $540 \times 361$  grid resolution ( $0.50^\circ \times 0.67^\circ$ ) and 42 pressure levels between the 1000 hPa and 0.1 hPa levels in the vertical.

## 3. Results

[8] The geographical location of the Himalayan mountain region in the Indian subcontinent is shown in Figure 1. The topography data are obtained from the Shuttle Radar Topography Mission (SRTM). More details of the project and system about SRTM can be found from Farr *et al.* [2007]. Figure 1 shows that the region between  $30^\circ\text{N}$ – $40^\circ\text{N}$  and  $60^\circ\text{E}$ – $90^\circ\text{E}$  is associated with highly complex topography with the height of the mountains reaching more than 3 km. Using the background removal method described in the section 2.1, Figure 2 shows AIRS L1B radiance (channel 75;  $667.78 \text{ cm}^{-1}$ ) perturbations obtained for both the ascending and descending passes (Figures 2a and 2b, respectively) of the Aqua satellite on 9 December 2008. The weighting function of the channel 75 peaks near 40 km in the stratosphere and the Full Width Half Maximum (FWHM) of this channel is  $\sim 12$  km. Figure 2a shows the wave perturbations observed in the stratosphere and it can be seen that the phase lines are aligned along the northwest and southeast directions at 07:59 UT (Universal Time) on 9 December 2008. Figure 2b shows the AIRS obtained radiance perturbations on the same day but at 21:41 UT. Both these (Figures 2a and 2b) indicate that the wave could have persisted for 12 h on 9 December 2008. It is known that mountain waves [Durrant,

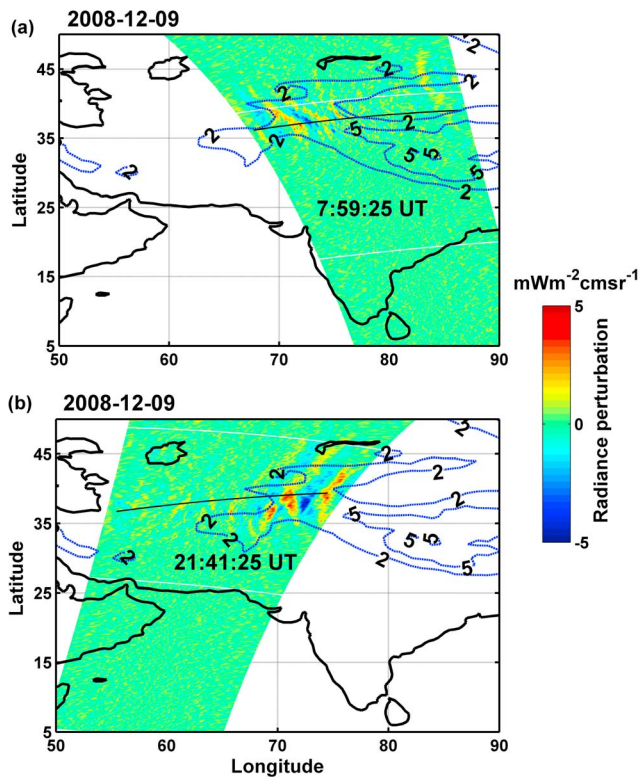


**Figure 2.** Radiance perturbations after removal of the background for the spectral channel  $667.78 \text{ cm}^{-1}$  on 9 December 2008 with overlaid topography contours for (a) ascending and (b) descending passes of AIRS satellite. The emission weighting function peaks around 40 km altitude. Topography contours at intervals of 3 km.

1986] are standing waves whose origin is can be related to the interaction of ambient synoptic flow with topography. In order to see the wave perturbations at lower heights, it has been taken different AIRS channels with weighting functions peak at different heights. For example, Figure 3 shows the radiance perturbations that are converted into temperature perturbations at different height levels for the event as shown in the Figure 2a. The AIRS channels that were used to obtain the perturbations as shown in Figures 3a–3d are  $2296.7 \text{ cm}^{-1}$ ,  $2316.9 \text{ cm}^{-1}$ ,  $2361.1 \text{ cm}^{-1}$ , and  $667.78 \text{ cm}^{-1}$  respectively. The temperature perturbations are obtained from radiance perturbations as each of the AIRS channels has unique radiance response for a given temperature perturbation [Hoffmann and Alexander, 2009]. Even though the amplitude of perturbations behave differently for the above different channels, mountain waves are seen (Figure 3) at different altitudes ( $\sim 18 \text{ km}$  to  $\sim 40 \text{ km}$ ) in the stratosphere over the same region. It is to be noted here that the daytime  $4 \mu\text{m}$  temperature channels have nonlocal thermodynamic equilibrium (non-LTE) effects caused by the excitation of  $\text{CO}_2$  molecules by the solar radiation [Hoffmann and Alexander, 2009]. For this reason, it is suggested to use the information obtained from these channels for the studies of nighttime gravity wave activities.

[9] Figures 4a and 4c show the horizontal projection of the wave events indicated in the Figures 2a and 2b, respectively. The projection in the Figure 4a (Figure 4c) is made with the origin lying in the west (east) of the swath. It can be noticed that the orientations of phase lines are different for the ascending and descending passes (Figure 4a and Figure 4c, respectively). One reason for this is that the change in the wind flow direction with altitude (directional wind shear) could change the wave phase structure [e.g., Eckermann et al., 2007]. Theoretical and modeling studies for circular 3-D obstacles predict that the shape, amplitude, and phase line orientation of the wave pattern vary with

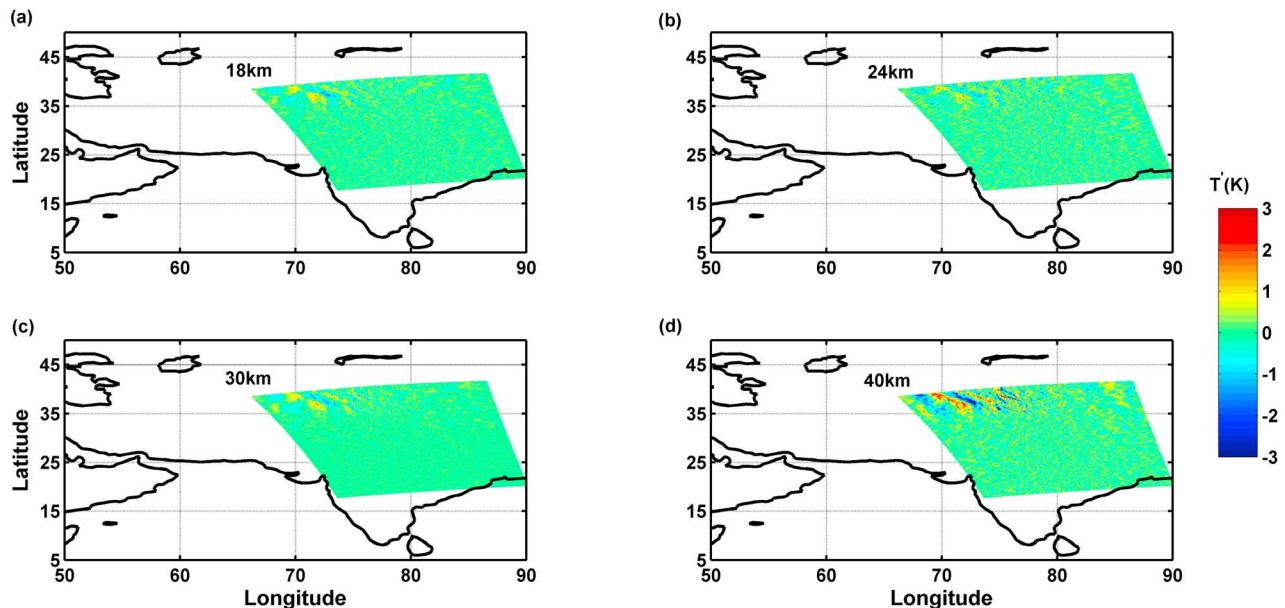


**Figure 3.** AIRS maps showing the temperature perturbations calculated from radiance perturbations at four different altitudes on 9 December 2008 at 07:59 UT.

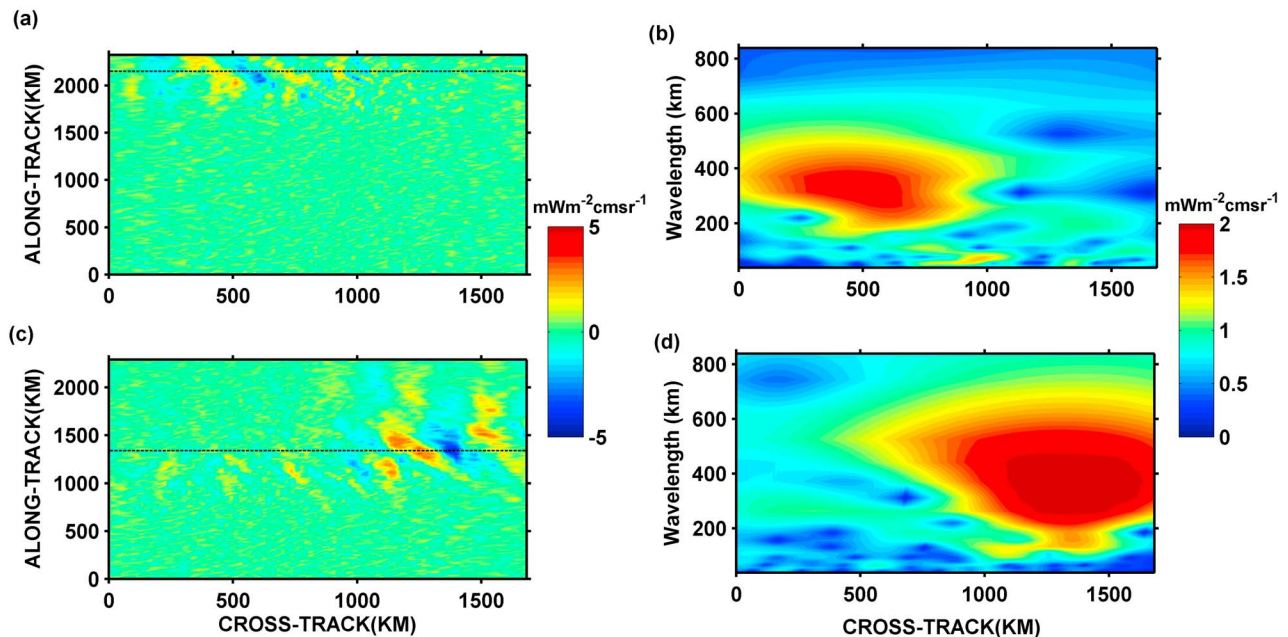


**Figure 4.** (a, b) Horizontal projection mountain wave event for ascending pass on 9 December 2008 at 07:59 UT and wavelet (Morlet) spectra of radiance perturbations along the dashed line indicated in Figure 4a, respectively. (c, d) Same as Figures 4a and 4b but for the descending pass, i.e., on 9 December 2008 at 21:41 UT. The projection in Figure 4a (Figure 4c) are made with origin point west (east) of real swath.

altitude [Eckermann *et al.*, 2007, and references therein]. In the present study, it is observed that the direction of the wind flows changes in the stratosphere (not shown) during the ascending and descending passes of the satellite. This might be the reason for the observed change of wave phase-line orientation between the Figures 4a and 4c. Figures 4b and 4d show the Morlet wavelet spectra (calculated along the dashed line indicated in the Figures 4a and 4c) of the wave event. The wavelet spectrum shows the peak of the horizontal (cross-track) wavelength lying between 200 and 500 km. To find the wave propagation vector, it has been used the harmonic analysis fitting for each of the cross-track rows of the AIRS granules. The harmonic fitting is done for the horizontal wavelengths starting from 37.8 km (the average cross-track-resolution of the AIRS granule is 18.9 km) up to 500 km. The chosen wavelength is a best fit to the data and the correlation is greater than 0.5. For the event shown in the Figure 4a, the obtained cross-track wavelength is 276 km. The amplitude and phase information can be obtained by fitting this wave to each cross-track row. The phase shift between dominant waves in the adjacent rows is proportional to the along-track wave number [Ern *et al.*, 2004; Alexander and Barnett, 2007]. In the present case, it has been obtained the along-track wavelength of 289 km and the direction of propagation of the wave of  $70^\circ$  clockwise from the east.

[10] As a supplement, use has also been made of the MLS data during the same period. Figures 5a and 5c show the MLS orbit track (filled circles) for the ascending (8.03 UT) and descending (21:44 UT) passes, respectively, for the same period of the AIRS observations. The orbit tracks are superimposed on the AIRS radiance maps shown in the Figure 5.

The temperature profiles along the orbital track are shown in Figures 5b and 5d. The profiles are running from the southeast (SE) to the northwest (NW) and from the southwest (SW) to the northeast (NE) for the ascending and descending passes, respectively. During the ascending pass, the MLS orbit track is away from the observed wave event whereas in the descending pass the track is close to the wave event. The temperature profiles shown in the Figure 5d clearly indicate the wave modulation in the stratosphere. Figure 6a shows temperature perturbations embedded on the topography map along the MLS orbit track (Figure 5c). The temperature perturbations are obtained by removing a fourth-order polynomial fit from the data. Figures 6b and 6c show the wavelet spectra of MLS and AIRS2 derived height profiles of temperature respectively near the latitude/longitude,  $40^\circ\text{N}/68^\circ\text{E}$ . Both the MLS and AIRS show the dominant wave vertical wavelength of  $\sim 25$  km in the stratosphere. Figure 6a indicates that the amplitude of the temperature wave perturbation is more than the radiance-measured temperature perturbations (Figure 3d) in the stratosphere, which is because the radiance measured value is a fraction of the true wave amplitude that depends on the AIRS frequency channel used [Alexander and Barnett, 2007]. In the present case, it has been taken the frequency  $667.7\text{ cm}^{-1}$  in the AIRS  $15\text{ }\mu\text{m}$  band and the fraction is  $\sim 0.75$ . The radiance-calculated wave perturbation is  $\sim 4$  K (Figure 3d) and the true amplitude of the wave is  $4/0.75 \approx 5$  K. To see whether this true amplitude is similar to what observed from the AIRS retrieval, it is plotted in Figures 7a and 7b the vertical cross-sections of the temperature amplitude, shown along the solid lines in Figures 2a and 2b, respectively. The maximum amplitude

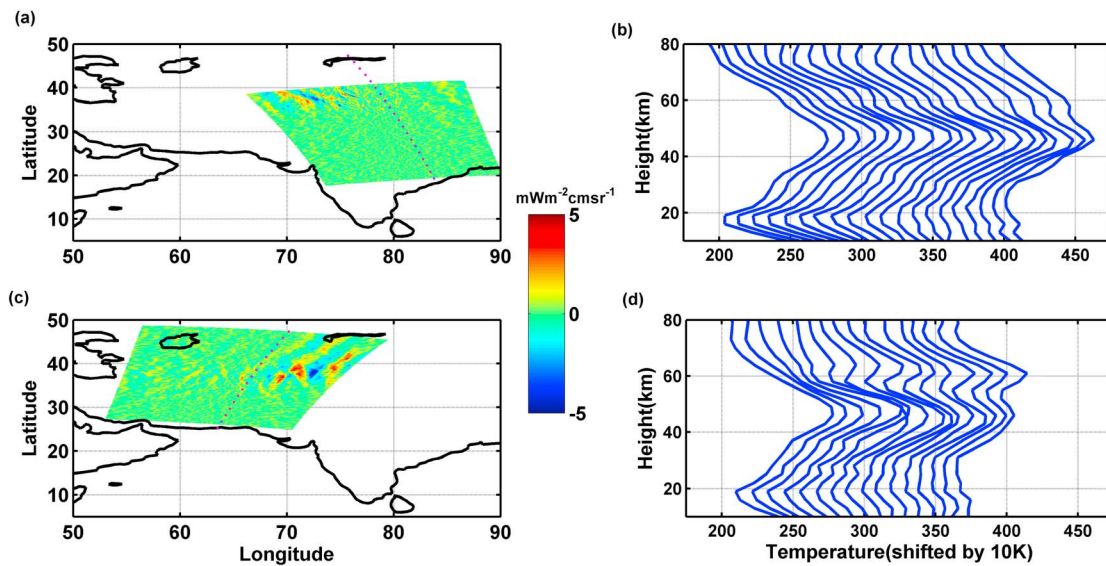


**Figure 5.** (a) Radiance anomalies for  $667.78 \text{ cm}^{-1}$  channel on 9 December 2008 at 07:59 UT and the MLS positions indicated as dotted lines. (b) Temperature profiles measured by MLS along solid circles running from southeast to northwest. (c, d) Same as Figures 5a and 5b but for the descending pass at 21:41 UT. The MLS profiles (Figure 5d) running from southwest to northeast. The MLS overpass timings 08:03 UT (Figure 5a) and 2144 UT (Figure 5c).

of the wave is found to be  $\sim 7 \text{ K}$ , which agrees with the AIRS L2 retrieval. However, the maximum amplitude of the wave is slightly larger in both the MLS-derived temperature (Figure 6a) and retrieved temperature (Figure 7a) comparing to the radiance measured true amplitude. The downward phase propagation of the wave observed in the Figure 7 implies that the energy of the wave is propagating upward. Sometimes the error in the AIRS L2 retrieved temperature is of the same order of magnitude of the true gravity wave induced temperature perturbations. Thus it is encouraged to use more sophisticated techniques [e.g., *Ern et al.*, 2004; *Hoffmann and Alexander*, 2009] for the retrieval of temperature from radiance measurements rather than making use of direct AIRS L2 products for gravity wave studies.

[11] Mountain waves generated in the troposphere can propagate up into the stratosphere under certain background meteorological conditions like nonexistence of zero winds. The general conditions for the generation and vertical propagation of mountain waves to higher levels are as follows: (1) strong low level winds in a stable atmosphere, which is required for inducing initial perturbations by wind flows over mountains, and (2) weak tropopause that allows waves to propagate through it into the stratosphere. The Himalayan mountain range lies in the subtropical high-pressure belt, where the seasonal meridional migration of the pressure and wind systems greatly alters the seasonal weather. During winter, the midlatitude westerlies sweep over this region, whereas during the monsoon months, in contrast to winters, the Himalaya is under the influence of easterlies. In the present case, it has been taken an event that occurred during the northern hemispheric winter month of December 2008, when the Himalaya was under the influence of the westerlies at all the levels. Figure 8 shows vector wind plots superimposed on the radiance perturbation shown in Figure 2a

at different stratospheric heights on 9 December 2008. The winds shown here are obtained from the NCEP/NCAR reanalysis data. It may be observed that the magnitude of the wind speed increases with height and in the stratosphere it reaches up to  $70 \text{ ms}^{-1}$  (Figure 8d).

[12] At lower levels (Figure 8a), it can be seen that the winds deviate from their original direction of westerlies. The complex orography of the Himalayan region (Figure 1) can easily deflect and decelerate the low-level flow. Figure 8b shows the vector winds near the mountaintops ( $\sim 4 \text{ km}$ ) and the maximum wind speed is  $\sim 19.6 \text{ ms}^{-1}$ . It is also observed that the wave phase fronts are oriented perpendicular to the wind vectors at this level. The maximum wind speed at the 300 hPa level is  $\sim 40 \text{ ms}^{-1}$ . Figure 8 indicates the favorable conditions for the mountain wave generation as the wind speed at the top of the mountain is  $\sim 20 \text{ ms}^{-1}$  and the wind speed gradually increases with altitude. As discussed previously, the approximate vertical wavelength visible to AIRS channels is  $>12 \text{ km}$ ; if a mountain wave propagates upstream at a speed greater than  $40 \text{ ms}^{-1}$ , it will be refracted to a vertical wavelength that is just longer than 12 km. The winds near the mountain top blow at the speed of  $19.6 \text{ ms}^{-1}$  perpendicular to the ridge line along the Himalayan mountain, supporting the orographic origin of the wave. A further supporting evidence of the wave event forced by topography will be provided in the following subsection.

### 3.1. MERRA Wind Fields

[13] In this section, we analyze the MERRA gridded ( $0.50^\circ \times 0.67^\circ$ ) reanalysis data distributed globally, in order to see the horizontal structure of the wave event on 9 December 2008 over the Himalayan mountain region. The NCEP/NCAR reanalysis data discussed previously is distributed globally with  $2.5^\circ \times 2.5^\circ$  grid resolutions.

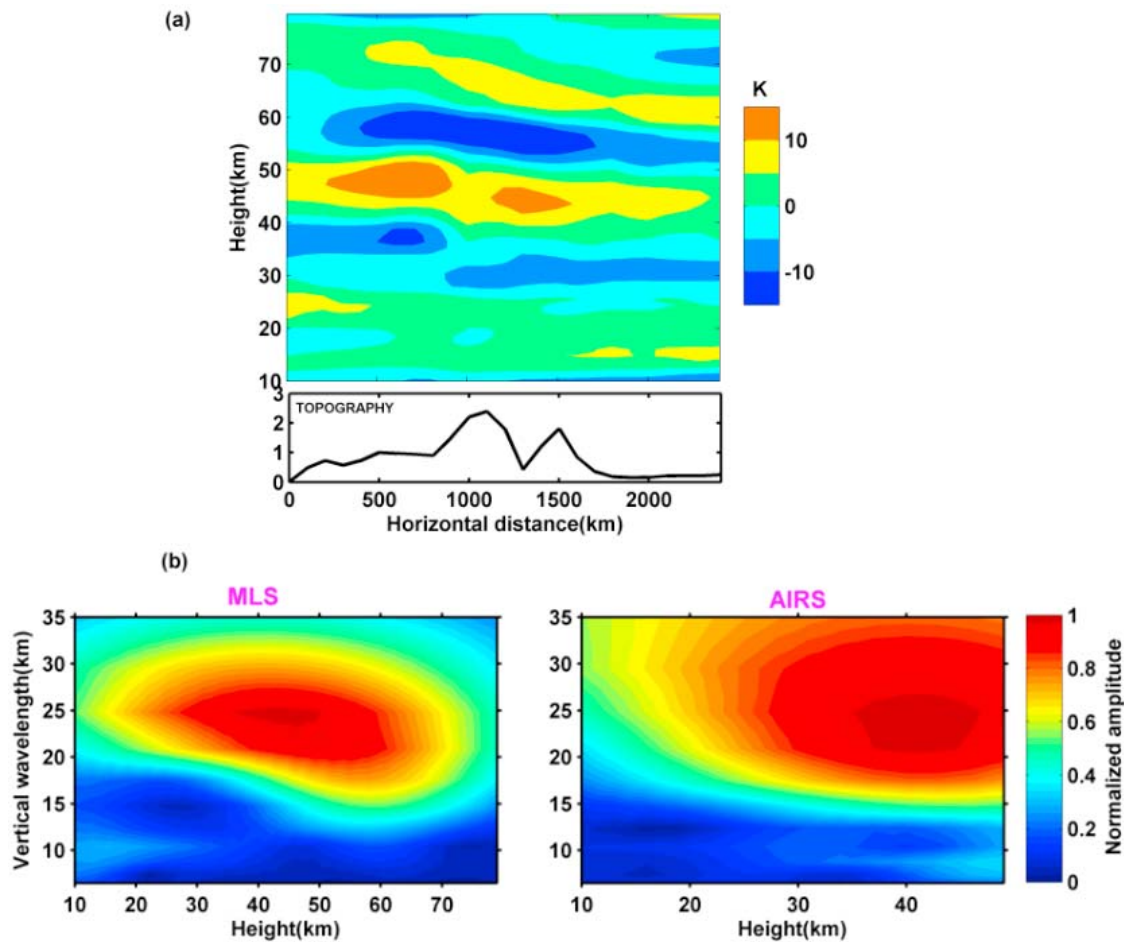


**Figure 6.** (a) The temperature anomalies measure by the MLS at the locations indicated as solid circles in Figure 5c. The profiles plotted as vertical cross sections as a function of horizontal distance (west to east, in kilometers). (b) Wavelet (Morlet) spectrum of vertical profile of temperature anomaly measured by MLS at 39.9°N, 67.5°E on 9 December 2008, 21:44 UT.

However, the wave event observed in this study could not be resolved with such a poor resolution. A high spatial resolution data set, such as MERRA, is needed to validate the wave event with observations. Since the MERRA data is globally distributed globally, we need to first remove the contribution from waves such as the global-scale planetary waves, tides, and other small-scale gravity waves. Hence we applied a Butterworth band-pass (150–500 km) filter has been applied to the MERRA horizontal wind fields and the wind divergences are calculated from the filtered winds. Figure 9 shows the horizontal structure of the wave in the wind divergence field (MERRA data) at 06 UT on 9 December 2008 in the altitudes of 5 km and 42 km. A shift in position of the wave toward the north is seen between the altitudes 5 km (Figure 9a) and 42 km (Figure 9b). The horizontal structure of the wave (Figure 9b) is similar to the AIRS observation (Figure 2a) at the stratospheric heights. To confirm this in the MERRA data, Figure 10 shows the wavelet spectrum of the divergence field at 42 km at the same time. It is noted that the observed maximum horizontal wavelength lying between 250 km and 450 km is similar to the AIRS observation in Figure 4. However, the peak horizontal wavelength in the MERRA is  $\sim 350$  km that is larger than the AIRS observed

horizontal wavelength, as the resolution of the MERRA data is coarser than the AIRS data. The AIRS data sample the wave event at a particular location only every 12 h, whereas the MERRA data can be obtained for every 6 h, thus making it easier to find the time evolution of the wave event. For example, Figure 11 shows the horizontal wind divergence at the 42 km altitude for four times, namely, 00, 06, 12, and 18 h UT. It is observed that the wave event is seen over the western Himalayan mountain region from 00 UT to 18 UT on 9 December 2008, further supporting the inference of orography generated wave event. This observation using the MERRA data indicates that it has the capability of simulating/assimilating this event in a reasonable manner.

[14] Another interesting point is that the vertical wavelength of a gravity wave generated potentially by airflowing over a terrain, subjected to the condition of constant stability, wind, and no rotation, is given by

$$(\lambda_z)_{theory} = \frac{2\pi U}{N} \quad (1)$$

where  $U$  is the mean wind speed and  $N$  is the Brunt-Väisälä frequency. The above equation indicates that for a given

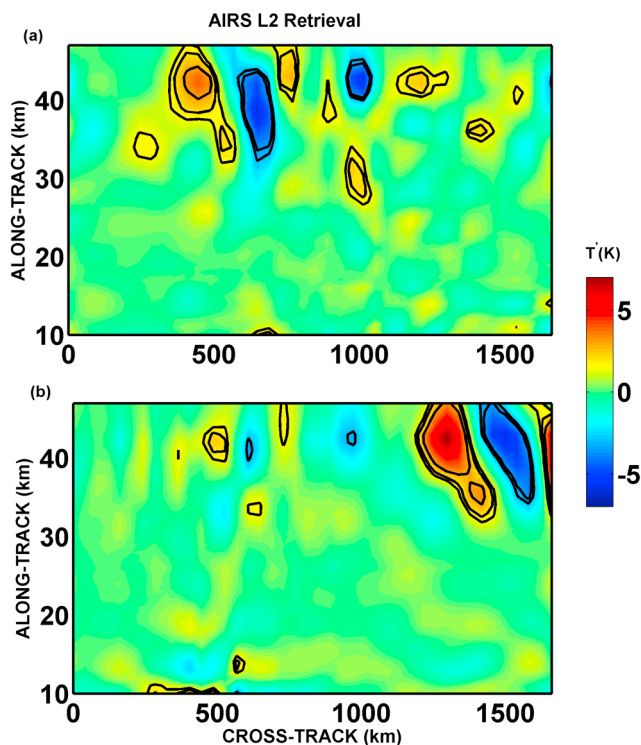


**Figure 7.** Cross section of AIRS retrieved temperature perturbations on 9 December 2008, at (a) 0759 UT and (b) 2141 UT. The location of cross section is shown in Figure 2 (solid line).

stability profile, an increasing (decreasing) cross-barrier flow results in mountain waves with longer (shorter) vertical wavelengths. Conversely, for a given cross-barrier flow, a

greater (lesser) stability can lead to mountain waves with shorter (longer) vertical wavelengths. Now from Figure 12, the wind speed at the stratospheric height of  $\sim 2$  hPa level is  $88 \text{ ms}^{-1}$  and the  $N$  value is  $0.0235$  per second. From the above equation, the calculated vertical wavelength (theory) is  $\sim 24$  km that is almost equal to the observed vertical wavelength of  $24.7$  km (Figure 6b) in the stratosphere. Thus the vertical wavelength of a stationary gravity wave in the stratosphere inferred from the AIRS as well as the MLS instruments agrees with the theoretical vertical wavelength calculated using the MERRA winds. Using the gravity wave dispersion relation, the estimated intrinsic frequency of the mountain wave in the stratosphere is  $\sim 2.1 \times 10^{-3} \text{ s}^{-1}$ . The measured 3-D wave numbers ( $k, l, m$ ) and the temperature amplitude can be used to deduce the absolute momentum flux of the waves using the following formula [Ern *et al.*, 2004]:

$$(M_x, M_y) = \frac{1}{2} \rho \left( \frac{g}{N} \right)^2 \left( \frac{\hat{T}}{T} \right)^2 \left( \frac{k}{m}, \frac{l}{m} \right) \quad (2)$$

where ( $k, l$ ) is the horizontal wave number,  $m$  is the vertical wave number, and  $\hat{T}$  is the temperature amplitude of the wave, and  $T$  is the background temperature. In the present case, from the observed wave properties near 40 km, the estimated values of ( $M_x, M_y$ ) are  $\sim (0.034 \text{ Pa}, 0.035 \text{ Pa})$ . The magnitude ( $\sim 0.05 \text{ Pa}$ ) of the momentum flux value estimated in the direction of wave propagation vector is in agreement with the other observed values reported elsewhere [e.g., Eckermann and Preusse, 1999; Preusse *et al.*, 2002; Alexander and Teitelbaum, 2007].

#### 4. Summary

[15] Using the observations made by the space-borne AIRS and MLS sounders on 9 December 2008 over the western

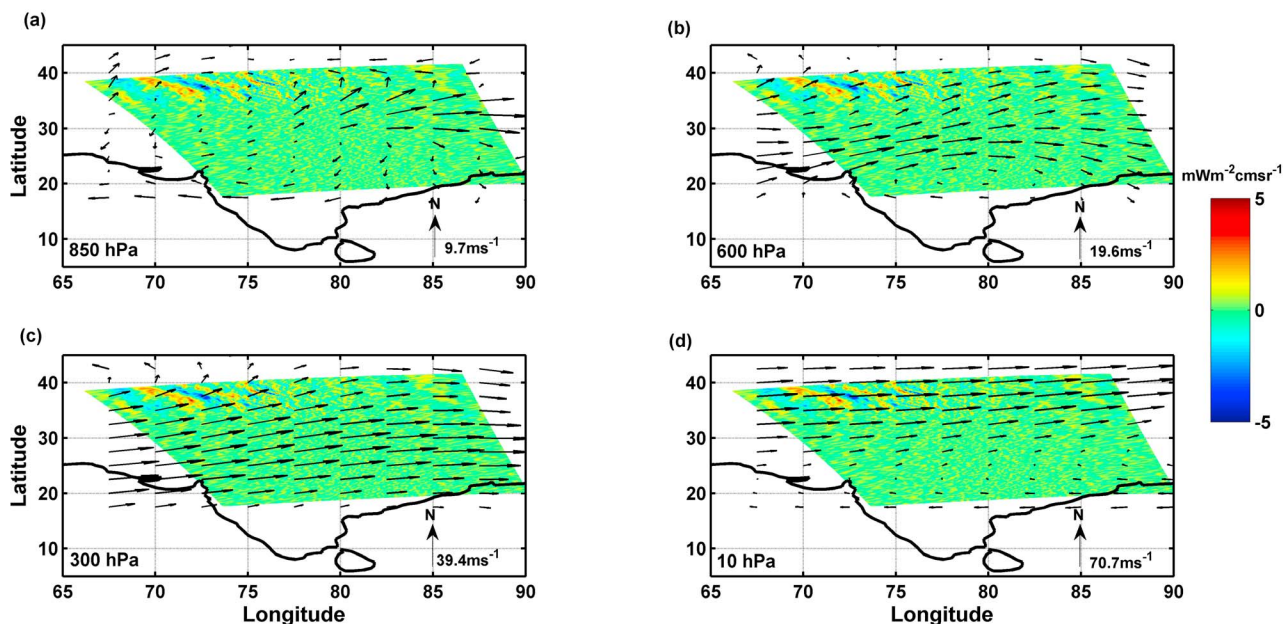


**Figure 8.** Geographic projection of the mountain wave event same as Figure 2a, superimposed by wind vectors from NCEP/NCAR reanalysis on 9 December 2008 at different pressure levels. The maximum wind speed at each pressure level is also indicated.

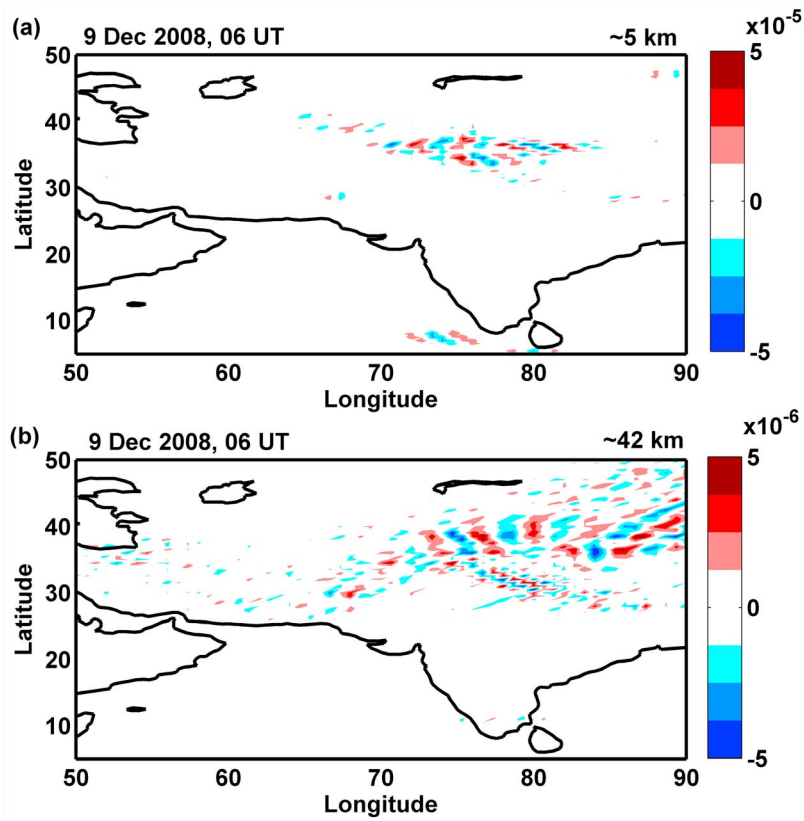


Figure 9. MERRA horizontal wind divergence on 9 December 2008 at 06 UT at (a) 5 km and (b) 42 km.

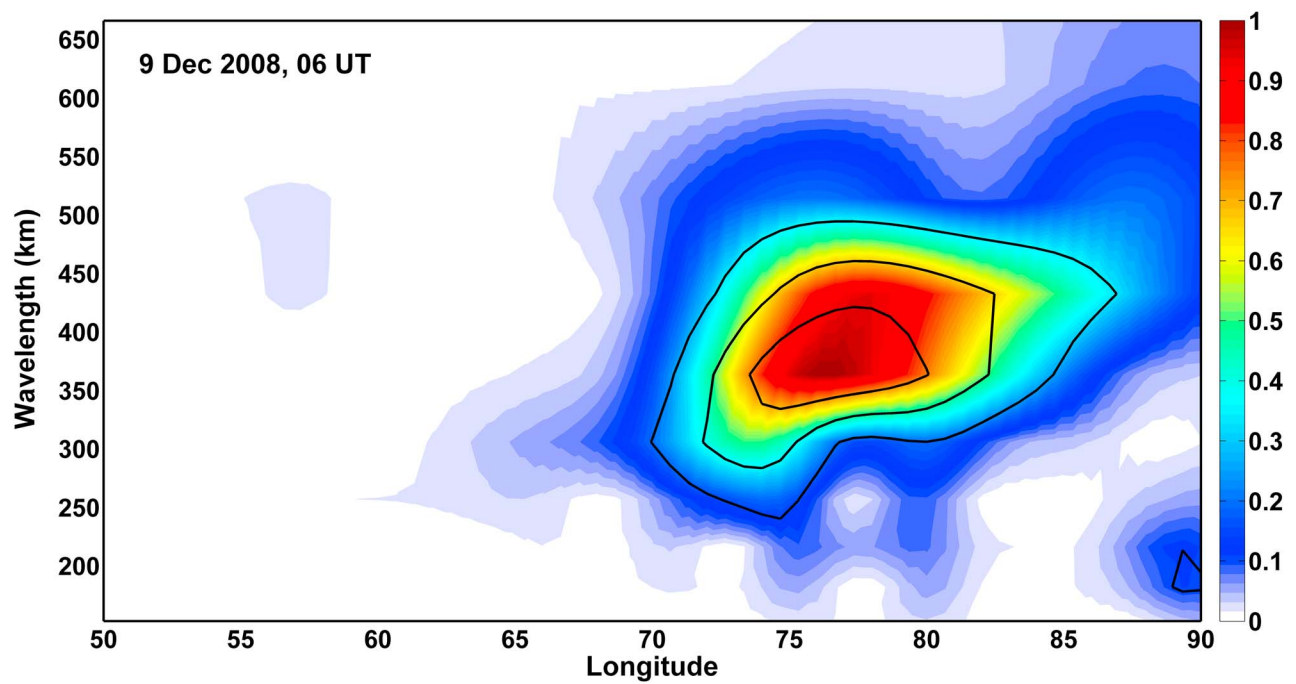
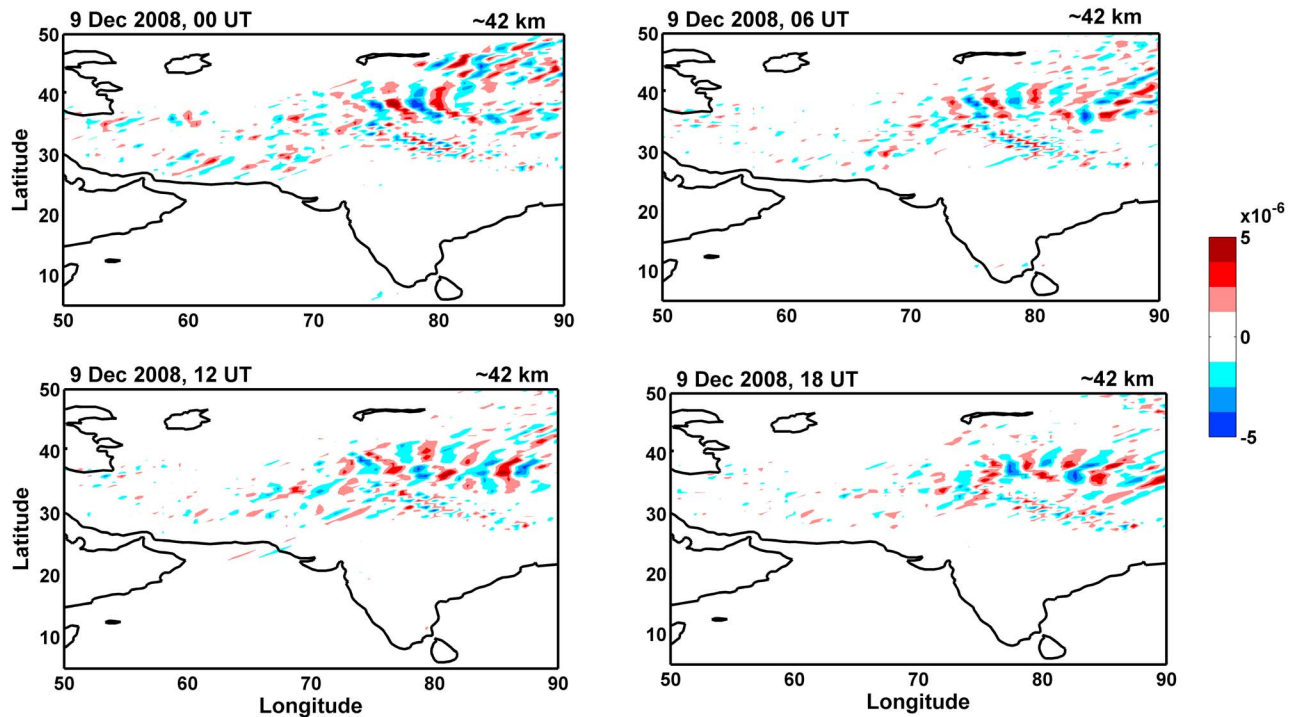


Figure 10. Wavelet Spectrum of horizontal wind divergence field at latitude  $38.5^{\circ}\text{N}$ . Contours indicate the 95% significant level.



**Figure 11.** MERRA horizontal wind divergence at 42 km at times 00, 06, 12, and 18 UT, respectively.

parts of the Himalayan region, the present study reports on the characteristics of mountain waves in the stratosphere. The Himalayan region is associated with complex topography and is a potential source for the generation of mountain waves when airflows over it, especially, during winter season of the northern hemisphere, when strong westerly winds persist at all heights in the troposphere over these latitudes. The AIRS observations during both the ascending and descending passes over this region show strong perturbations in the stratospheric temperature on 9 December 2008. The observed horizontal ( $\lambda_x$ ,  $\lambda_y$ ) and vertical ( $\lambda_z$ ) wavelengths are 276 km, 289 km, and  $\sim 25$  km, respectively. The measured radiance perturbations are converted into temperature perturbations and the errors are corrected for the vertical wavelength depending attenuation factor as suggested by *Alexander and Barnett* [2007]. The corrected amplitude agrees well with the AIRS retrieval and MLS derived temperature perturbations during the same period of observation. It is also observed that the wind vectors at the mountaintop were oriented perpendicular to the wave phase fronts and the magnitude of the wind speed consistently increased with height. The wave amplitudes are found to increase with horizontal wind speed above  $40 \text{ ms}^{-1}$ , and hence the wave event observed in the present study is considered to be primarily forced by topography. It is also noticed that the wave event is stationary in time on 9 December 2008 above the western Himalayan mountain region, further supporting the inference of orographic origin of the wave event. It is noticed that the MERRA reanalysis data has the capability of reasonable simulating/assimilating this mountain wave event. Also shown is the close agreement between the observed (MERRA winds) and theoretical vertical wavelengths of a stationary gravity wave propagating up into

the stratosphere. Using the observed 3-D properties of the wave event, the estimated momentum flux values are in good agreement with the other values of large-amplitude mountain wave events reported elsewhere. In this regard, the present study is considered to be an important ingredient in the gravity wave parameterization schemes, as the Tibetan plateau and the adjacent Himalayan topography are not dealt properly the current GCMs.

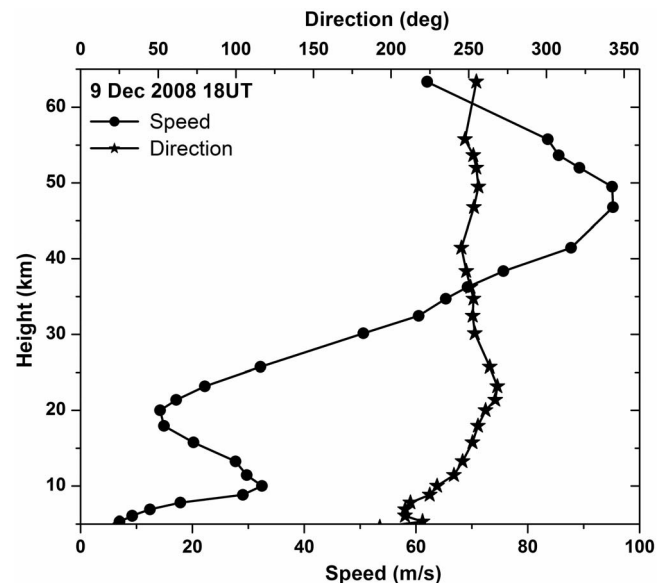


**Figure 12.** Horizontal wind components obtained from MERRA Reanalysis data at latitude/ longitude:  $37.5^\circ\text{N}/72.0^\circ\text{E}$ , on 9 December 2008 at 18 UT.

[16] **Acknowledgments.** This work is supported by the Department of Space, Government of India. The data used in this effort were acquired as part of the activities of NASA's Science Mission Directorate and are archived and distributed by the Goddard Earth Sciences (GES) Data and Information Services Center (DISC). We are also extremely thankful to the Global Modeling and Assimilation Office (GMAO) and the GES DISC for the dissemination of MERRA data.

## References

- Alexander, M. J., and C. Barnett (2007), Using satellite observations to constrain gravity wave parameterizations for global models, *J. Atmos. Sci.*, *64*, 1652–1665, doi:10.1175/JAS3897.1.
- Alexander, M. J., and H. Teitelbaum (2007), Observation and analysis of a large amplitude mountain wave event over the Antarctic Peninsula, *J. Geophys. Res.*, *112*, D21103, doi:10.1029/2006JD008368.
- Alexander, M. J., and H. Teitelbaum (2011), Three-dimensional properties of Andes mountain waves observed by satellite: A case study, *J. Geophys. Res.*, *116*, D23110, doi:10.1029/2011JD016151.
- Alexander, M. J., et al. (2008), Global estimates of gravity wave momentum flux from High Resolution Dynamics Limb Sounder observations, *J. Geophys. Res.*, *113*, D15S18, doi:10.1029/2007JD008807.
- Alexander, M. J., S. D. Eckermann, D. Broutman, and J. Ma (2009), Momentum flux estimates for South Georgia Island mountain waves in the stratosphere observed via satellite, *Geophys. Res. Lett.*, *36*, L12816, doi:10.1029/2009GL038587.
- Aumann, H. H., D. T. Gregorich, S. L. Gaiser, D. F. Hagan, T. S. Pagano, L. L. Strow, and D. Ting (2000), AIRS level 1b algorithm theoretical basis document (ATBD) part 1 (IR), technical report, NASA, Washington, D. C. [Available at [http://eosps.gsf.nasa.gov/eos\\_homepage/for\\_scientists/atbd](http://eosps.gsf.nasa.gov/eos_homepage/for_scientists/atbd).]
- Aumann, H., et al. (2003), AIRS/AMSU/HSB on the Aqua mission: Design, science objectives, data products, and processing systems, *IEEE Trans. Geosci. Remote Sens.*, *41*, 253–264, doi:10.1109/TGRS.2002.808356.
- Bacmeister, J. T. (1993), Mountain-wave drag in the stratosphere and mesosphere inferred from observed winds and a simple mountain wave parameterization scheme, *J. Atmos. Sci.*, *50*, 377–399, doi:10.1175/1520-0469(1993)050<0377:MWDITS>2.0.CO;2.
- Baines, P. G. (1995), *Topographic Effects in Stratified Flows*, Cambridge Univ. Press, Cambridge, U. K.
- Barros, A. P., G. Kim, E. Williams, and S. W. Nesbitt (2004), Probing orographic controls in the Himalayas during the monsoon using satellite imagery, *Nat. Hazards Earth Syst. Sci.*, *4*, 29–51, doi:10.5194/nhess-4-29-2004.
- Blumen, W. (Ed.) (1990), *Atmospheric Processes Over Complex Terrain*, *Meteorol. Monogr.*, vol. 45, Am. Meteorol. Soc., Boston, Mass.
- Boos, W. R., and Z. Kuang (2010), Dominant control of South Asian monsoon by orographic insulation versus Plateau heating, *Nature*, *463*, 218–222, doi:10.1038/nature08707.
- Carlsaw, K. S., et al. (1998), Increased stratospheric ozone depletion due to mountain induced atmospheric waves, *Nature*, *391*, 675–678, doi:10.1038/35589.
- Choi, H.-J., H.-Y. Chun, J. Gong, and D. L. Wu (2012), Comparison of gravity wave temperature variances from ray-based spectral parameterization of convective gravity wave drag with AIRS observations, *J. Geophys. Res.*, *117*, D05115, doi:10.1029/2011JD016900.
- Dornbrack, A., M. Leutbecher, J. Reichardt, A. Behrendt, K. P. Müller, and G. Baumgarten (2001), Relevance of mountain wave cooling for the formation of polar stratospheric clouds over Scandinavia: Mesoscale dynamics and observations for January 1997, *J. Geophys. Res.*, *106*, 1569–1582, doi:10.1029/2000JD900194.
- Durrant, D. R. (1986), Mountain waves, in *Mesoscale Meteorology and Forecasting*, edited by P. Ray, pp. 472–492, Am. Meteorol. Soc., Boston, Mass.
- Eckermann, S. D., and P. Preusse (1999), Global measurements of stratospheric mountain waves from space, *Science*, *286*, 1534–1537, doi:10.1126/science.286.5444.1534.
- Eckermann, S. D., A. Dornbrack, S. Vosper, H. Flentje, M. J. Mahoney, T. P. Bui, and K. S. Carlsaw (2006), Mountain wave-induced polar stratospheric cloud forecasts for aircraft science flights during SOLVE/ THESEO 2000, *Weather Forecast.*, *21*, 42–68, doi:10.1175/WAF901.1.
- Eckermann, S. D., M. Jun, D. L. Wu, and D. Broutman (2007), A three-dimensional mountain wave imaged in satellite radiance throughout the stratosphere: Evidence of the effects of directional wind shear, *Q. J. R. Meteorol. Soc.*, *133*, 1959–1975, doi:10.1002/qj.187.
- Ern, M., P. Preusse, M. J. Alexander, and C. D. Warner (2004), Absolute values of gravity wave momentum flux derived from satellite data, *J. Geophys. Res.*, *109*, D20103, doi:10.1029/2004JD004752.
- Farr, T. G., et al. (2007), The Shuttle Radar Topography Mission, *Rev. Geophys.*, *45*, RG2004, doi:10.1029/2005RG000183.
- Fetzer, E. J., and J. C. Gille (1994), Gravity wave variance in LIMS temperatures. Part I: Variability and comparison with background winds, *J. Atmos. Sci.*, *51*, 2461–2483, doi:10.1175/1520-0469(1994)051<2461:GWVILT>2.0.CO;2.
- Fritts, D. C., and M. J. Alexander (2003), A review of gravity wave dynamics and effects on the middle atmosphere, *Rev. Geophys.*, *41*(1), 1003, doi:10.1029/2001RG000106.
- Froidevaux, L., et al. (2008), Validation of Aura Microwave Limb Sounder stratospheric ozone measurements, *J. Geophys. Res.*, *113*, D15S20, doi:10.1029/2007JD008771.
- Fueglistaler, S., S. Buss, B. P. Luo, H. Wernli, H. Flentje, C. A. Hostetler, L. R. Poole, K. S. Carlsaw, and T. Peter (2003), Detailed modeling of mountain wave PSCs, *Atmos. Chem. Phys.*, *3*, 697–712, doi:10.5194/acp-3-697-2003.
- Gong, J., D. L. Wu, and S. D. Eckermann (2011), Gravity wave variances and propagation derived from AIRS radiances, *Atmos. Chem. Phys. Discuss.*, *11*, 11691–11738, doi:10.5194/acpd-11-11691-2011.
- Haynes, P. (2005), Stratospheric dynamics, *Annu. Rev. Fluid Mech.*, *37*, 263–293, doi:10.1146/annurev.fluid.37.061903.175710.
- Hoffmann, L., and M. J. Alexander (2009), Retrieval of stratospheric temperatures from Atmospheric Infrared Sounder radiance measurements for gravity wave studies, *J. Geophys. Res.*, *114*, D07105, doi:10.1029/2008JD011241.
- Holton, J. R. (1982), The role of gravity wave induced drag and diffusion in the momentum budget of the mesosphere, *J. Atmos. Sci.*, *39*, 791–799, doi:10.1175/1520-0469(1982)039<0791:TROGWI>2.0.CO;2.
- Jiang, Y. B., et al. (2007), Validation of the Aura Microwave Limb Sounder Ozone by ozonesonde and lidar measurements, *J. Geophys. Res.*, *112*, D24S34, doi:10.1029/2007JD008776.
- Kim, Y.-J., S. D. Eckermann, and H. Chun (2003), An overview of the past, present and future of gravity wave drag parameterization for numerical climate and weather prediction models, *Atmos. Ocean*, *41*, 65–98, doi:10.3137/ao.41.0105.
- Lindzen, R. S. (1981), Turbulence and stress owing to gravity wave and tidal breakdown, *J. Geophys. Res.*, *86*, 9707–9714, doi:10.1029/JC086iC10p09707.
- Livesey, N. J., et al. (2007), Version 2.2 level 2 data quality and description document, *JPL D-33509*, 115 pp., Jet Propul. Lab., Pasadena, Calif. [Available at [http://mls.jpl.nasa.gov/data/2.2\\_data\\_quality\\_document.pdf](http://mls.jpl.nasa.gov/data/2.2_data_quality_document.pdf)]
- Mann, G. W., K. S. Carlsaw, M. P. Chipperfield, S. Davies, and S. D. Eckermann (2005), Large nitric acid trihydrate particles and denitrification caused by mountain waves in the Arctic stratosphere, *J. Geophys. Res.*, *110*, D08202, doi:10.1029/2004JD005271.
- McLandress, C. (1998), On the importance of gravity waves in the middle atmosphere and their parameterization in general circulation models, *J. Atmos. Sol. Terr. Phys.*, *60*, 1357–1383, doi:10.1016/S1364-6826(98)00061-3.
- Molnar, P., W. R. Boos, and D. S. Battisti (2010), Orographic controls on climate and paleoclimate of Asia: Thermal and mechanical roles for the Tibetan Plateau, *Annu. Rev. Earth Planet. Sci.*, *38*, 77–102, doi:10.1146/annurev-earth-040809-152456.
- Nastrom, G. D., and D. C. Fritts (1992), Sources of mesoscale variability of gravity waves. 1. Topographic excitation, *J. Atmos. Sci.*, *49*, 101–110, doi:10.1175/1520-0469(1992)049<0101:SOMVOG>2.0.CO;2.
- Pierce, R. B., et al. (2003), Large-scale chemical evolution of the Arctic vortex during the 1999/2000 winter: HALOE/POAM III Lagrangian photochemical modeling for the SAGE III/Ozone Loss and Validation Experiment (SOLVE) campaign, *J. Geophys. Res.*, *108*(D5), 8317, doi:10.1029/2001JD001063.
- Pitts, M. C., L. R. Poole, A. Dornbrack, and L. W. Thomason (2011), The 2009–2010 Arctic polar stratospheric cloud season: A CALIPSO perspective, *Atmos. Chem. Phys.*, *11*, 2161–2177, doi:10.5194/acp-11-2161-2011.
- Preusse, P., A. Dornbrack, S. D. Eckermann, M. Riese, B. Schaeler, J. T. Bacmeister, D. Broutman, and K. U. Grossmann (2002), Space-based measurements of stratospheric mountain waves by CRISTA: 1. Sensitivity, analysis method, and a case study, *J. Geophys. Res.*, *107*(D23), 8178, doi:10.1029/2001JD000699.
- Queney, P. (1947), Theory of perturbations in stratified currents with applications to air flow over mountain barriers, *Misc. Rep. 23*, Dept. of Meteorol., Univ. of Chicago, Chicago, Ill.
- Rienecker, M. M., et al. (2007), The GEOS-5 Data Assimilation System—Documentation of Versions 5.0.1 and 5.1.0, Technical Report Series on Global Modeling and Data Assimilation, *NASA Tech. Memo. NASA/TM-2007-104606*, vol. 27, 92 pp., NASA Goddard Space Flight Cent., Greenbelt, Md.

- Rienecker, M. M., et al. (2011), MERRA: NASA's Modern-Era Retrospective Analysis for Research and Applications, *J. Clim.*, *24*, 3624–3648, doi:10.1175/JCLI-D-11-00015.1.
- Schwartz, M. J., et al. (2008), Validation of the Aura Microwave Limb Sounder temperature and geopotential height measurements, *J. Geophys. Res.*, *113*, D15S11, doi:10.1029/2007JD008783.
- Siskind, D. E., S. D. Eckermann, L. Coy, J. P. McCormack, and C. E. Randall (2007), On recent interannual variability of the Arctic winter mesosphere: Implications for tracer descent, *Geophys. Res. Lett.*, *34*, L09806, doi:10.1029/2007GL029293.
- Smith, R. B. (1979), The influence of mountains on the atmosphere, *Adv. Geophys.*, *21*, 87–230, doi:10.1016/S0065-2687(08)60262-9.
- Smith, R. B. (1989), Hydrostatic flow over mountains, *Adv. Geophys.*, *31*, 1–41, doi:10.1016/S0065-2687(08)60052-7.
- Smith, R. B., S. Skubis, J. D. Doyle, A. Broad, and H. Volkert (2002), Mountain waves over Mont Blanc: Influence of a stagnant boundary layer, *J. Atmos. Sci.*, *59*, 2073–2092, doi:10.1175/1520-0469(2002)059<2073:MWOMBI>2.0.CO;2.
- Trenberth, K. E., and S.-C. Chen (1988), Planetary waves kinematically forced by Himalayan orography, *J. Atmos. Sci.*, *45*, 2934–2948, doi:10.1175/1520-0469(1988)045<2934:PWKFBH>2.0.CO;2.
- Tsuda, T., M. Nishida, C. Rocken, and R. Ware (2000), A global morphology of gravity wave activity in the stratosphere revealed by the GPS occultation data (GPS/MET), *J. Geophys. Res.*, *105*(D6), 7257–7274, doi:10.1029/1999JD901005.
- Waters, J. W., et al. (2006), The Earth Observing System Microwave Limb Sounder (EOS MLS) on the Aura satellite, *IEEE Trans. Geosci. Remote Sens.*, *44*(5), 1075–1092, doi:10.1109/TGRS.2006.873771.
- Wu, D. L. (2004), Mesoscale gravity wave variances from AMSU-radiances, *Geophys. Res. Lett.*, *31*, L12114, doi:10.1029/2004GL019562.
- Wu, D. L., and J. W. Waters (1996), Gravity-wave-scale temperature fluctuations seen by the UARS MLS, *Geophys. Res. Lett.*, *23*, 3289–3292, doi:10.1029/96GL02924.
- Wu, D. L., and F. Zhang (2004), A study of mesoscale gravity waves over the North Atlantic with satellite observations and a mesoscale model, *J. Geophys. Res.*, *109*, D22104, doi:10.1029/2004JD005090.
- Wurtele, M. G., R. D. Sharman, and A. Datta (1996), Atmospheric lee waves, *Annu. Rev. Fluid Mech.*, *28*, 429–476, doi:10.1146/annurev.fl.28.010196.002241.